

A fast infrared radiative transfer model based on the adding–doubling method for hyperspectral remote-sensing applications

Zhibo Zhang^a, Ping Yang^{a,*}, George Kattawar^b, Hung-Lung (Allen) Huang^c,
Thomas Greenwald^c, Jun Li^c, Bryan A. Baum^d, Daniel K. Zhou^e, Yongxiang Hu^e

^a*Department of Atmospheric Sciences, Texas A&M University, College Station, TX 77843, USA*

^b*Department of Physics, Texas A&M University, College Station, TX, 77843, USA*

^c*CIMSS/University of Wisconsin-Madison, WI, USA*

^d*Space Science and Engineering Center, University of Wisconsin-Madison, WI, USA*

^e*NASA Langley Research Center, USA*

Received 23 June 2006; received in revised form 3 January 2007; accepted 4 January 2007

Abstract

A fast infrared radiative transfer (RT) model is developed on the basis of the adding–doubling principle, hereafter referred to as FIRTM-AD, to facilitate the forward RT simulations involved in hyperspectral remote-sensing applications under cloudy-sky conditions. A pre-computed look-up table (LUT) of the bidirectional reflection and transmission functions and emissivities of ice clouds in conjunction with efficient interpolation schemes is used in FIRTM-AD to alleviate the computational burden of the doubling process. FIRTM-AD is applicable to a variety of cloud conditions, including vertically inhomogeneous or multilayered clouds. In particular, this RT model is suitable for the computation of high-spectral-resolution radiance and brightness temperature (BT) spectra at both the top-of-atmosphere and surface, and thus is useful for satellite and ground-based hyperspectral sensors. In terms of computer CPU time, FIRTM-AD is approximately 100–250 times faster than the well-known discrete-ordinate (DISORT) RT model for the same conditions. The errors of FIRTM-AD, specified as root-mean-square (RMS) BT differences with respect to their DISORT counterparts, are generally smaller than 0.1 K.

© 2007 Elsevier Ltd. All rights reserved.

Keywords: Hyperspectral; Radiative transfer; Clouds; Adding–doubling; Remote sensing; Fast model

1. Introduction

The high-spectral-resolution or hyperspectral sensors in the infrared (IR), e.g., the Atmospheric Infrared Sounder (AIRS) [1], the Cross-Track Infrared Sounder [2], the Infrared Atmospheric Sounding Interferometer (IASI) [3,4] and the Atmospheric Emitted Radiance Interferometer (AERI) [5,6], provide a wealth of

*Corresponding author. Tel.: +1 979 845 4923; fax: +1 979 862 4466.

E-mail address: pyang@ariel.met.tamu.edu (P. Yang).

information about the atmosphere, land and oceans, and therefore offer an unprecedented opportunity for the study of the earth–atmosphere system. At the same time, the analysis of the resulting hyperspectral data poses new challenges to the efficiency and accuracy of the current radiative transfer (RT) modeling capabilities. As an essential component in the implementation of the retrieval and data assimilation algorithms based on hyperspectral measurements, a RT model must be computationally efficient, and yet have appropriate accuracy and general applicability under all conditions. For clear-sky atmospheres, a number of fast RT models have been developed, e.g., the optical path transmittance [7], the stand-alone RT algorithm [8], the optimal spectral sampling model (OSS) [9] and the principal-component-based RT model [10].

Global analysis of data from the High-Resolution Infrared Radiometer Sounder (HIRS) indicates that approximately 65–70% of the Earth's surface is generally covered by clouds. The HIRS field of view (FOV) is approximately 18 km at nadir. It is estimated that only 6.5% of the HIRS footprints are “clear-sky” [11]. For AIRS, which has a slightly smaller FOV than HIRS with a spatial resolution of approximately 15 km at nadir, only 4.5% of the data over ocean have mean residual cloud fraction less than 0.6% [12]. Therefore, RT models for cloudy conditions, which can account for both the absorption of the atmospheric gases and the scattering and absorption of cloud particles, are required for cloud clearing [13], cloud property retrieval [14,15] and satellite data assimilation [16] from hyperspectral measurements. In previous research, a simplified cloudy RT model coupled with the OSS model has been employed in a newly developed inversion algorithm for dealing with both clear and cloudy radiances in retrieving atmospheric and cloud parameters [17]. The primary objective of this work is to develop an accurate, flexible and efficient radiative transfer equation (RTE) solver that can be easily coupled with a clear-sky model to provide a complete and efficient RT computational package for applications to hyperspectral remote sensing.

The multiple-scattering term in the RTE is responsible for the difficulty associated with the development of an efficient RTE solver. The numerical computation of this term not only determines the complexity and accuracy of a RT model but also has a direct impact on its computational efficiency. Because multiple scattering in the IR spectral region is not as strong as in the shortwave spectral region, this complex process is largely simplified, if not ignored altogether, in most IR remote-sensing applications. For example, the upwelling radiances at the top of the atmosphere (TOA) in the IR region for a completely overcast FOV have been approximated in the literature as follows [18–22]:

$$I_{\text{TOA}} = \varepsilon B(T_c) + (1 - \varepsilon)I_0, \quad (1)$$

where I_{TOA} is the radiance at the TOA, B is the Planck function, T_c is the cloud temperature, I_0 is the radiance reaching the cloud base and ε is cloud emissivity that is usually assumed to be $1 - \exp(-\tau_a/\mu)$ where τ_a is the optical thickness of the cloud due to the absorption and μ is the cosine of the viewing angle. Due to the neglect of cloud reflection in Eq. (1), some thermal energy that should have been reflected back to the surface penetrates through the cloud as an artifact in the simulation, resulting in an overestimation of the radiances at TOA.

For inferring cloud height and optical thickness from satellite observations, Minnis et al. [23,24] developed an efficient RT model by parameterizing the TOA visible reflectance and IR emittance using the look-up tables (LUTs) of cloud reflectances and emittances under various cloud microphysical and optical conditions. To facilitate the retrieval of ice cloud optical thickness and effective particle size from AIRS data, Wei et al. [15] developed a fast infrared RT model (hereafter, FIRT M1) to compute the TOA radiances for a cloudy atmosphere containing a single-layered, homogenous and isothermal cloud. With a pre-computed LUT for cloud reflectance and transmittance, FIRT M1 is approximately three orders of magnitude faster than the well-known discrete-ordinate (DISORT) model developed by Stamnes et al. [25]. FIRT M1 is based essentially on an extension of Eq. (1). In addition to the two terms on the right-hand side of Eq. (1), two additional terms representing the thermal emission by the atmosphere above the cloud and the corresponding reflection by the cloud are also taken into account in FIRT M1. Most recently, Niu et al. [26] extended the FIRT M1 to two-layered cloudy atmospheres (FIRT M2) by adding several more terms to Eq. (1). The above models are computationally efficient and also more accurate than the simple approximation in Eq. (1) due to the consideration of multiple scattering. However, the flexibility of these models is limited because the RTEs were simplified to obtain optimal efficiency for a particular type of application, specifically computations of TOA radiances for which there are only one or at most two homogenous and isothermal cloud layers. Therefore,

these models cannot be applied to retrieval implementations involving multilayered clouds or ground-based measurements.

Many robust and rigorous RT models have been developed that can fully account for multiple scattering, such as the discrete-ordinate method [25,27,28], the spherical harmonics method [29], the Monte Carlo method [30,31] and the adding–doubling method [32–39]. Although these models have been widely used in narrowband remote-sensing applications, the computational burden of applying them directly to a broader spectral range with a fine resolution is unlikely to be computationally affordable in practice. However, with some modification of the algorithms to account for the computational requirements of hyperspectral computations, the efficiency of these models can be improved substantially. For example, Moncet and Clough [40] developed a fast RT model using the adding–doubling method, referred to as Code for High-resolution Accelerated Radiative Transfer with Scattering (CHARTS), to interpret observations of water clouds for a high-spectral-resolution AERI. The advantage of CHARTS is that the time-consuming doubling step is performed only at selected wavelengths in a given spectral region of interest. The bulk radiative properties of the cloud layer for other wavelengths are interpolated from the computed ones. This modification of the adding–doubling algorithm is feasible due to the fact that the scattering properties of water droplets vary with the wavelength much more smoothly than the absorption of atmospheric gases. Although CHARTS is much faster than DISORT, the doubling and interpolation step still uses more than half of the total CPU time. This computational burden is expected to increase for ice cloud applications because the strong forward scattering of ice particles requires the use of more Legendre terms in the expansion of the phase function and consequently more streams for the adding–doubling operations.

High-level ice clouds comprise as much as 30% of the cloud cover [41,42] and play an important and yet not well-understood role in the climate system [43,44]. A fast and yet robust RT model with general applicability can be quite useful not only for hyperspectral remote-sensing applications but also for satellite data assimilation and climate study. Inspired by the virtues of FIRT M1/FIRT M2 and CHARTS, we develop a new fast infrared radiative transfer model based on the adding–doubling principle (FIRT M-AD) with an emphasis on applications to ice clouds. The methodology of FIRT M-AD is described in Section 2. The cloud realization scheme used in FIRT M-AD is discussed in Section 3. The development of a LUT for ice cloud radiative properties for FIRT M-AD is given in Section 4. In Section 5, we show the accuracy of FIRT M-AD in some typical applications. Finally, a brief summary of the present study is given in Section 6.

2. Methodology of FIRT M-AD

For a vertically inhomogeneous, multilayered, plane-parallel atmosphere as shown in Fig. 1, we need both a clear-sky RT model that accounts for the molecular absorption and a numerical RTE solver that accounts for the multiple-scattering in cloud and aerosol layers. The adding–doubling method is a rigorous method that has

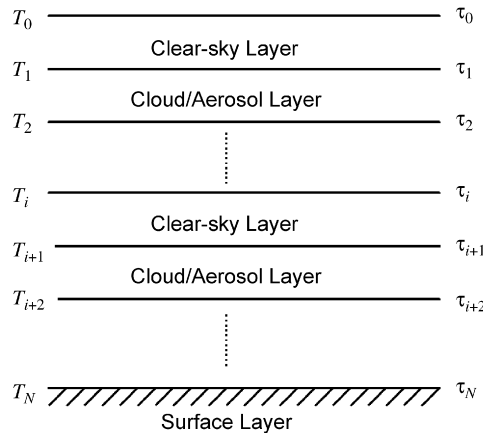


Fig. 1. A vertically inhomogeneous, absorptive and scattering, multilayered, plane-parallel atmosphere.

been used extensively in the development of numerical RTE solvers for plane-parallel atmospheres [32–39]. The basics of the adding–doubling method and its application to RT in the thermal IR region are outlined in Appendix A. As discussed in the appendix, for the spectral region considered in the present study, i.e., 800–1300 cm^{−1}, the azimuthally dependent solar contribution to the sensor observations is insignificant [14,15,26], so that only the azimuthally averaged bidirectional reflection ($\bar{\mathbf{R}}$) and transmission ($\bar{\mathbf{T}}$) matrices and the thermal emission vector (\mathbf{E}) (see Appendix A for their definitions) are required for the adding–doubling method. To obtain these properties for cloud/aerosol layers (note that the clear-sky layers have an analytical solution), the doubling method can be used. In this method, a cloud/aerosol layer in Fig. 1 is first divided into a number of identical sub-layers. The optical thicknesses of the sub-layers are very small ($\tau_k \sim 2^{-10}$) [45–47], so that their $\bar{\mathbf{R}}_k$, $\bar{\mathbf{T}}_k$ and emissivity vector, \mathbf{e}_k (the subscript k indicates that the property is associated with the k th sub-layer) may be obtained analytically from the cloud bulk scattering properties, i.e., the extinction efficiency ($\langle Q_e \rangle$), scattering albedo ($\langle \varpi \rangle$) and phase function ($\langle P \rangle$), under the single-scattering approximation. Because each sub-layer is isothermal, its thermal emission \mathbf{E}_k is simply $\mathbf{e}_k B(T_k)$, where T_k is the temperature of the sub-layer. Finally, the $\bar{\mathbf{R}}$, $\bar{\mathbf{T}}$ and \mathbf{E} of entire cloud/aerosol layer are obtained by adding at each step two identical layers, i.e., the doubling process (see Appendix A for details). Although the computational efficiency of the doubling method is sufficient for computations at a small number of spectral wavelengths, the computational burden increases greatly if a few hundred or even thousands of wavelengths are involved such as in the case of hyperspectral remote sensing.

The intent of FIRTM-AD is to reduce the computational burden associated with the doubling process, whereas the model still retains the robustness and high accuracy that the adding–doubling method offers. This is achieved through the use of an extensive pre-computed LUT of $\bar{\mathbf{R}}$, $\bar{\mathbf{T}}$ and \mathbf{e} for various ice clouds in conjunction with efficient interpolation schemes in the model. Following CHARTS [40], FIRTM-AD computes the $\bar{\mathbf{R}}$, $\bar{\mathbf{T}}$ and \mathbf{e} of clouds only at a few dozens of selected spectral points in the LUT. The $\bar{\mathbf{R}}$, $\bar{\mathbf{T}}$ and \mathbf{e} at other wavelengths (wavenumbers) in the interested spectral region are efficiently interpolated from the computed ones. At the selected spectral points, the burden associated with the computations of cloud $\bar{\mathbf{R}}$, $\bar{\mathbf{T}}$ and \mathbf{e} is also alleviated by the use of the pre-computed LUT. In FIRTM-AD, if a cloud is homogenous in terms of bulk scattering properties, then its $\bar{\mathbf{R}}$ and $\bar{\mathbf{T}}$ are either directly obtained or interpolated from the pre-computed LUT, and therefore the doubling process may be avoided. An inhomogeneous cloud is implemented in FIRTM-AD by superposition of homogenous sub-layers. For the computation of thermal emission by non-isothermal clouds, the doubling method described above is also used in FIRTM-AD. However, due to the use of the pre-computed LUT, the non-isothermal cloud can be divided into much thicker and therefore fewer sub-layers, leading to a much faster doubling process in FIRTM-AD than in the conventional adding–doubling method. The implementation of non-isothermal clouds in FIRTM-AD and the computation of their thermal emission will be discussed in the next section.

The applicability of the pre-computed LUT in RT models is a consequence of the fact that only three parameters, namely the incident wavelength (λ) or wavenumber (ν), cloud optical thickness (τ) and effective particle size (D_e) are sufficient to determine the $\bar{\mathbf{R}}$, $\bar{\mathbf{T}}$ and \mathbf{e} of a cloud layer in most remote-sensing implementations and RT simulations [48,49]. A limitation of the LUT-based RT models such as FIRTM-AD and FIRTM1/FIRTM2, is that, while they may be computationally efficient, the applicability of these models is confined by the scope of the cloud conditions built into the LUT. Use of a pre-computed LUT also raises the issue pertaining to the accuracy of the models, because interpolation is required to obtain the cloud properties that are not explicitly specified at the LUT grid points. The development of the pre-computed LUT for FIRTM-AD and the accuracy of FIRTM-AD will be discussed later.

3. Cloud realization scheme in FIRTM-AD

FIRTM-AD is a numerical RTE solver developed to account for the multiple-scattering process in cloud layers. Similar to other RTE solvers such as DISORT [25], FIRTM-AD depends on the availability of an accurate clear-sky RT model to account for the molecular absorption and provide an optical thickness profile of the background atmosphere. This directly leads to the issue of cloud realization, or more broadly, how to insert the cloud/aerosol layers into the background atmosphere. As illustrated in Fig. 2a, a physically sound scheme is to assume that the cloud and atmospheric gases coexist in a model layer (hereafter, referred to as

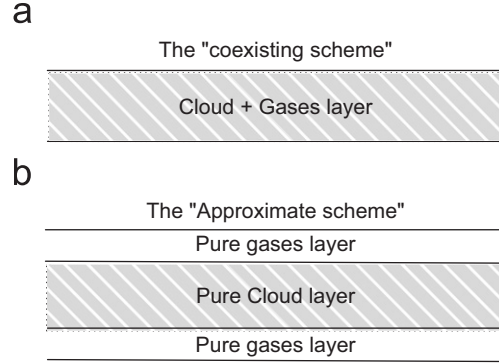


Fig. 2. (a) Schematic illustration of the “coexisting scheme”, (b) and the “approximate scheme”, which is used in FIRTM-AD as an approximation to the “coexisting scheme”.

“coexisting scheme”). In the RTE, the coexistence results in the increase of the optical thickness and the decrease of the single-scattering albedo of a cloud–gas coexisting model layer in comparison with a layer consisting solely of cloud particles, due to the absorption of the atmospheric gases. The total optical thickness, τ_{layer} , and the albedo, ϖ_{layer} , of cloud–gases coexisting model layer in Fig. 2a can be expressed as

$$\tau_{\text{layer}} = \tau_{\text{gas}} + \tau_{\text{cloud}}, \quad (2a)$$

$$\varpi_{\text{layer}} = \frac{\varpi_{\text{cloud}}}{1 + \tau_{\text{gas}}/\tau_{\text{cloud}}}, \quad (2b)$$

where τ_{cloud} and ϖ_{cloud} are the optical thickness and albedo of a layer consisting solely of cloud particles, respectively. The variable τ_{gas} is the optical thickness of the background atmosphere. It is straightforward to implement the “coexisting scheme” by redefining optical thickness and albedo of the layer according to Eq. (2a) in an RT model that explicitly computes the cloud bulk radiative properties, such as DISORT. However, it is difficult to implement the “coexisting scheme” in FIRTM-AD, because it is impractical to develop a LUT of $\bar{\mathbf{R}}$, $\bar{\mathbf{T}}$ and ε for cloud–gas coexisting layers due to a wide range of variations of the τ_{gas} in Eq (2). Instead, the LUT in FIRTM-AD is for pure cloud layers only and the approach (hereafter referred to as the “approximate scheme”) illustrated in Fig. 2b is used to derive the $\bar{\mathbf{R}}$, $\bar{\mathbf{T}}$ and ε of a cloud–gas coexisting layer from the LUT for pure clouds and a given value of τ_{gas} . In this approach, the cloud layer is specified at the middle level of a background atmosphere layer. In the current version of FIRTM-AD, the optical thicknesses of the upper and lower pure gas layers are specified as $\tau_{\text{gas}}/2$.

Another important cloud realization issue in FIRTM-AD as well as in other IR RT models is how to implement a non-isothermal cloud. Observations show that even cirrus clouds can have a non-negligible physical thickness [50]. As a result, there may be a considerable temperature difference between the cloud top and cloud base. An IR-based RT model should be able to simulate this temperature variation within the cloud to account for its effect on the thermal emission of the cloud. In the conventional adding–doubling model, because a cloud layer is divided into a large number of thin sub-layers to initialize the doubling process, the cloud temperature structure can be easily implemented by assigning a different temperature to each sub-layer. The thermal emission of the entire cloud layer can be obtained through the doubling process. However, the computational cost of the conventional doubling method is usually unaffordable for hyperspectral computations. To alleviate the computational burden associated with the doubling process, we assume that when the cloud optical thickness is smaller than some threshold value τ^* (by default set to 20 in FIRTM-AD) the effect of internal cloud temperature structure on the cloud thermal emission is insignificant. Under this assumption, the thermal emission of a cloud with optical thickness smaller than τ^* can be decomposed into two parts as follows:

$$\mathbf{E}(\tau, \langle \varpi \rangle, \langle P \rangle, T_{\text{top}}, T_{\text{bot}}) \approx \varepsilon[\tau, \langle \varpi \rangle, \langle P \rangle] \mathcal{B}[(T_{\text{top}} + T_{\text{bot}})/2], \quad (3)$$

where T_{top} and T_{bot} are the cloud top and cloud bottom temperature, respectively. Based on the above assumption, a cloud with τ smaller than τ^* is treated as isothermal in FIRTM-AD and the corresponding thermal emission is obtained from Eq. (3) with a cloud emissivity of ϵ obtained from the LUT. If not explicitly specified otherwise by the user, a cloud with τ larger than τ^* is treated as non-isothermal in FIRTM-AD. To obtain the thermal emission, the cloud is first divided into sub-layers so that each sub-layer has an optical thickness of τ^* and only one sub-layer carries the residual. Note that all sub-layers are actually isothermal, but their temperatures are different from each other for simulating the temperature variation within the cloud. The temperature of each sub-layer is obtained from the user-specified temperature-optical thickness ($T(\tau)$) relationship for the cloud (by default a linear $T(\tau)$ is assumed). The emissivity ϵ_k of each sub-layer is obtained from the LUT and then the emission is obtained using Eq. (3). Finally, the thermal emission of the entire cloud layer is computed by doubling and adding the sub-layers. The threshold value, τ^* , determines the number of sub-layers into which a given non-isothermal cloud is divided in FIRTM-AD, and therefore the efficiency and accuracy of FIRTM-AD in the computation of thermal emission from non-isothermal clouds. A large value of τ^* allows FIRTM-AD to avoid most of the doubling process and therefore makes the model computationally efficient, but on the other hand limits the ability of FIRTM-AD to describe the cloud temperature variation for a cloud layer having an optical thickness smaller than τ^* . In FIRTM-AD, τ^* is a user-definable parameter that can be changed to meet different requirements. Note that τ^* is set to 20 in the results shown later. As approximations to general and realistic conditions, both the “approximate scheme” for the cloud insertion and the treatment of the non-isothermal clouds are error sources in FIRTM-AD. The errors associated with these approximations will be assessed later in Section 5.

4. Development of the pre-computed LUT for FIRTM-AD

As an essential part of FIRTM-AD, the pre-computed LUT is a set of databases containing the $\bar{\mathbf{R}}$, $\bar{\mathbf{T}}$ and ϵ of the retrieval object, such as ice clouds, water clouds and aerosol layers, in a discretized space of wavenumber (ν), optical thickness (τ) and effective particle size (D_e). The coverage and the resolution of the LUT are highly application-oriented and should be determined according to the retrieval object, retrieval algorithm and required accuracy.

The FIRTM-AD presented in this study is developed primarily for the inference of ice cloud properties from hyperspectral IR observations. The corresponding spectral coverage of the current LUT is from 800 to 1300 cm^{-1} . This atmospheric window region is chosen because of its importance in ice cloud property retrieval [14,15,51]. A hyperspectral sensor may have hundreds of channels over this region. However, because cloud bulk scattering properties vary slowly with wavenumber compared with the absorption of the atmospheric gases, it is unnecessary to build a LUT at the spectral resolution of the sensor [40]. Currently, only 39 spectral grid points from 800 to 1300 cm^{-1} are specified in the LUT.

The coverage over τ is currently chosen from 0.01 to 10, which corresponds to the sensitivity range of the IR sensors to the cloud optical thickness [14,52]. Thirty values within this region are specified in the LUT. An important point to note is that the optical thickness in the database of FIRTM-AD, i.e., from 0.01 to 10, is referenced to the optical thickness of a cloud at a visible wavelength of 0.55 μm . The IR optical thickness of cloud, τ_ν at a given wavenumber, ν , can be written in terms of visible optical thickness, τ_{vis} , as follows:

$$\tau_\nu = \frac{\langle Q_e(\nu) \rangle}{\langle Q_e(0.55 \mu\text{m}) \rangle} \tau_{\text{vis}}, \quad (4)$$

where $\langle Q_e \rangle$ is the bulk extinction efficiency [53]. In the current version of FIRTM-AD, we assume that $\langle Q_e(0.55 \mu\text{m}) \rangle$ is approximately 2.

The effective particle size, D_e , of an ice cloud is defined as follows [53]:

$$D_e = \frac{3 \int_0^\infty (\sum_i V_i(D) w_i(D)) n(D) dD}{2 \int_0^\infty (\sum_i A_i(D) w_i(D)) n(D) dD}, \quad (5)$$

where D is the maximum dimension of an ice particle, V_i is the volume of the ice particle with a given shape (i.e., habit) indicated by the index i , A_i is the projected area of randomly oriented ice particle with the i th habit,

Table 1

Quadrature points of 32-stream double-Gaussian quadrature over the upward hemisphere and the corresponding zenith angles

#	Quadrature point	Zenith angle (deg)
1	0.0053	89.6964
2	0.0277	88.4120
3	0.0672	86.1477
4	0.1223	82.9753
5	0.1911	78.9852
6	0.2710	74.2767
7	0.3592	68.9490
8	0.4525	63.0962
9	0.5475	56.8039
10	0.6408	50.1484
11	0.7290	43.1967
12	0.8089	36.0077
13	0.8777	28.6336
14	0.9328	21.1219
15	0.9723	13.5202
16	0.9947	5.9013

w_i is the habit distribution and $n(D)$ is the particle size distribution (PSD). Based on the analysis of in situ observations of ice cloud PSDs obtained in focused field campaigns over past few decades, an extensive database for ice cloud bulk scattering properties has been developed by Baum et al. [53]. This database contains the $\langle Q_e \rangle$, $\langle \varpi \rangle$ and $\langle P \rangle$ of various ice clouds with D_e from 10 to 180 μm over the spectral region from 100 to 3250 cm^{-1} with a resolution of 1 cm^{-1} . A similar approach was used to develop narrowband models that are currently being used for the moderate resolution imaging spectroradiometer (MODIS) operational ice cloud property retrieval [54]. The D_e coverage of the LUT for FIRTM-AD is consistent with the above database, i.e., from 10 to 180 μm with a resolution of 10 μm .

At each grid point of the LUT, the dimension and nature of $\bar{\mathbf{R}}$, $\bar{\mathbf{T}}$ matrices and $\boldsymbol{\varepsilon}$ vectors are determined by the angular coordinate discretization scheme used for the adding–doubling implementation. In the current version of FIRTM-AD, the double-Gaussian quadrature described by Stamnes [25] with 32 quadrature points, i.e., 32-stream (16 for the upward hemisphere and 16 for the downward hemisphere) is used for the coordinate discretization. The values of the quadrature points and corresponding zenith angles are listed in Table 1. Correspondingly, $\bar{\mathbf{R}}$ and $\bar{\mathbf{T}}$ are 16×16 matrices, whereas $\boldsymbol{\varepsilon}$ is a 16-element vector in the LUT. Note that the use of 8 or 16 streams would be accurate enough for most computations in the region from 800 to 1300 cm^{-1} . A relatively high order of the discrete-ordinate approximation is used in the present study. It ensures the accuracy of the model in some extreme cases and, in addition, this 32-stream LUT can be used to generate the libraries where fewer streams are needed.

After the grid points are specified and the angular discretization scheme chosen, the $\bar{\mathbf{R}}$, $\bar{\mathbf{T}}$ and $\boldsymbol{\varepsilon}$ on the grids of the LUT are computed using DISORT [25] with delta-M scaling [55]. The bulk scattering properties of ice clouds, i.e., $\langle Q_e \rangle$, $\langle \varpi \rangle$ and $\langle P \rangle$, are from Baum et al.’s database [53]. Then, the $\bar{\mathbf{R}}$, $\bar{\mathbf{T}}$ and $\boldsymbol{\varepsilon}$ are organized into three binary databases that together form the LUT used in FIRTM-AD. To obtain the $\bar{\mathbf{R}}$, $\bar{\mathbf{T}}$ and $\boldsymbol{\varepsilon}$ of clouds that are not specified in the LUT, interpolation is required. For simplicity and computational efficiency, a linear interpolation scheme is used in FIRTM-AD for all cloud radiative properties.

5. Accuracy estimation of FIRTM-AD

In this section, we assess the accuracy of FIRTM-AD in the computation of high-spectral-resolution (0.1 cm^{-1}) brightness temperature (BT) spectra at both the surface and TOA for various cloud and viewing geometry conditions. The accuracy is estimated by comparing the simulations from FIRTM-AD with those from the DISORT model under the same conditions.

Before proceeding to detailed error analyses, it is helpful to first have an overview of the differences between DISORT and FIRTm-AD in the model configurations for the following simulations. For the cloud realization, the “coexisting scheme” is used in DISORT whereas the “approximate scheme” is used in FIRTm-AD. As discussed in Section 3, the ability of FIRTm-AD in the implementation of non-isothermal clouds is limited by the threshold value τ^* . In DISORT, cloud bulk radiative properties, i.e., eigenvalues and eigenvectors [25], are computed at every spectral point specified by the given spectral (800–1300 cm^{-1}) region and resolution (0.1 cm^{-1}). In FIRTm-AD, cloud bulk radiative properties, i.e., $\bar{\mathbf{R}}$, $\bar{\mathbf{T}}$ and $\bar{\mathbf{e}}$, are computed only at 39 selected spectral points in the LUT. The properties at other points are interpolated from the computed ones. In both DISORT and FIRTm-AD, the 32-stream double-Gaussian quadrature is used for the discretization of angular coordinate. Note that the errors of DISORT in the interpolation of radiances from the model angles to the user-specified angles are negligible due to the use of a relatively high order of the discrete-ordinate approximation (32-stream). Therefore, based on the above comparisons, if DISORT is taken as the benchmark model, the errors in FIRTm-AD arise primarily from four major sources: (1) the error caused by using the cloud realization scheme discussed in Section 2 to approximate the non-isothermal and gas–cloud coexisting layer (hereafter referred to as the “cloud-realization error”); (2) the error caused by the interpolation of $\bar{\mathbf{R}}$, $\bar{\mathbf{T}}$ and $\bar{\mathbf{e}}$ over wavenumber ν (hereafter referred to as the “ ν -interpolation error”); (3) the error caused by the interpolation of $\bar{\mathbf{R}}$, $\bar{\mathbf{T}}$ and $\bar{\mathbf{e}}$ over τ (hereafter referred to as the “ τ -interpolation error”); (4) the error caused by the interpolation of radiances from the model angles specified by the angular discretization scheme to the user-specified angles (hereafter referred to as the “ μ -interpolation error”). As a reminder, the scheme currently used in FIRTm-AD for the interpolation of radiances from model angles to the user-specified angle is described in Appendix B. Note that the relative importance of above four error sources is different under different cloud and viewing conditions. As a result, the accuracy of FIRTm-AD is sensitive to both the cloud conditions and the sensor viewing angles. Because of the endless possibilities of these conditions in addition to the high computational cost of using DISORT to simulate the hyperspectral BT spectrum, a “complete” error analysis for FIRTm-AD is not provided. The strategy for the present accuracy estimation is to set up both “good” and “bad” scenarios, in terms of the number of error sources involving in FIRTm-AD, so that the relative importance of error sources can be estimated through comparisons between scenarios. In this fashion, the overall error level of FIRTm-AD can be estimated from the “bad” scenarios in which all error sources are considered.

In the present accuracy estimation the following two standards are used. The errors of FIRTm1 and FIRTm2, in terms of the root-mean-square (RMS) BT errors, for BT spectrum computations at TOA are on the order of 0.5 K over the spectral region 800–1300 cm^{-1} [15,26]. As a more comprehensive and rigorous model, FIRTm-AD should have an error level lower than 0.5 K. The sensitivity of the hyperspectral sensors, to which the FIRTm-AD could be potentially applied, can also be used as the standard for accuracy estimation. The NEdT (Noise Equivalent Differential Temperature) of current hyperspectral sounders, such as AIRS and IASI, are at the level of 0.2 K [4,56]. In our view, an acceptable error level for FIRTm-AD would be a value at or lower than the NEdT of above sensors (i.e., 0.2 K).

A tropical atmosphere is used in the present simulations with FIRTm-AD and DISORT. The atmosphere column from the surface to a height of 100 km above the surface is divided into 100 layers. The physical thickness of each layer varies from 0.5 to 2.5 km. The optical thickness of each layer due to the absorption of the atmospheric gases is obtained from the line-by-line radiative transfer model [57] with a resolution of 0.1 cm^{-1} . The temperature profile and optical depth profile at 1176.5 cm^{-1} (8.5 μm), 909.1 cm^{-1} (11 μm) and 833.3 cm^{-1} (12 μm) of this atmosphere are shown in Fig. 3. The planetary surface is assumed to be Lambertian. The surface temperature T_s is assumed as 299.7 K. Additionally, a surface albedo of $\alpha_s = 0.03$ is assumed regardless of wavenumber.

Fig. 4 shows the results from application of FIRTm-AD to the computation of high-spectral-resolution (0.1 cm^{-1}) BT spectra at TOA under single-layered cloud conditions. In this case, a cirrus cloud is located between 13.5 and 14.0 km above the surface. The cloud top and base temperatures are, respectively, 211.75 and 215.25 K. Fig. 4a shows BT spectra simulated from FIRTm-AD for various combinations of cloud visible optical thicknesses, τ_{vis} (0.10, 0.55 and 0.95) and satellite viewing angles, θ_v (5.9° and 45°) while the effective particle size, D_e , is assumed as 30 μm in all simulations. Fig. 4c shows the BT spectra from FIRTm-AD for various combinations of D_e (20-, 40- and 60 μm) and θ_v (5.9° and 45°) while τ_{vis} is assumed as 0.55 in all

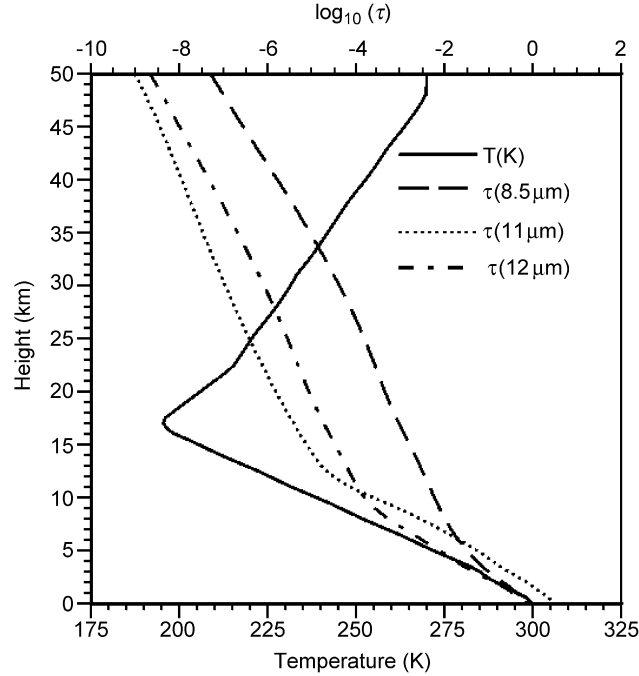


Fig. 3. Temperature profile and the optical depth profiles at 8.5, 11 and 12 μm of the background atmosphere used in the computations.

simulations. The above combinations of τ_{vis} , D_e and θ_v are chosen so that both “good” and “bad” scenarios are included in Fig. 4. For example, the scenario where $\tau_{\text{vis}} = 0.1$ and $\theta_v = 5.9^\circ$ is a “good” scenario in comparison with the one where $\tau_{\text{vis}} = 0.55$ and $\theta_v = 45^\circ$. This is because $\tau_{\text{vis}} = 0.1$ is on the grid of τ_{vis} space of the LUT, while $\tau_{\text{vis}} = 0.55$ is not, and $\theta_v = 5.9^\circ$ is a model angle, while $\theta_v = 45^\circ$ is not (see Table 1). As a result, no interpolation over τ_{vis} or θ_v is needed in FIRTm-AD for the former scenario but both are necessary for the latter. The BT spectra in Figs. 4a and c show considerable sensitivity to both τ_{vis} and D_e . These sensitivities have been used to infer the optical properties of thin cirrus clouds using the hyperspectral observations from AIRS [14,15]. The differences in the BT spectra (ΔBT spectra) between FIRTm-AD and DISORT in the scenarios in Figs. 4a and c are shown, respectively, in Figs. 4b and d. ΔBT is defined as follows:

$$\Delta\text{BT} = \text{BT}_{\text{FIRTm-AD}} - \text{BT}_{\text{DISORT}}. \quad (6)$$

The RMS value of the ΔBT spectrum is used as an index for the overall error level of FIRTm-AD following previous studies [15,26]. The RMS value is defined as

$$\text{RMS}(\Delta\text{BT}) = \sqrt{\frac{\sum_i^{N_p} (\Delta\text{BT}_i)^2}{N_p}}, \quad (7)$$

where N_p is the number of spectral points in the spectrum and ΔBT_i is the difference of BT between FIRTm-AD and DISORT at the i th spectral point. The RMS values of each ΔBT spectrum in Figs. 4b and d are listed in Table 2. The featureless ΔBT spectra in Figs. 4b and d indicate that the errors of FIRTm-AD are spectrally uncorrelated. The ΔBT spectra in Fig. 4d are almost identical to each other, revealing that the errors are independent of D_e . As shown in Table 2, the largest error, 0.0498 K, occurs in a “bad” scenario (scenario #8 in Table 2) where $\tau_{\text{vis}} = 0.55$, $D_e = 60 \mu\text{m}$ and $\theta_v = 45^\circ$. It is interesting to note that the error in the other “bad” scenario (scenario #4 in Table 2) where $\tau_{\text{vis}} = 0.95$, $D_e = 30 \mu\text{m}$ and $\theta_v = 45^\circ$, is only 0.0334 K. This is reasonable and can be explained as follows: because the τ_{vis} interpolation uses the adjacent points in the LUT, the relative errors of interpolation are similar at $\tau_{\text{vis}} = 0.55$ and 0.95. However, because the absolute value of the transmissivity of the former is larger than the latter, the absolute error of τ_{vis} interpolation in the former scenario is larger than the latter leading to the results in Table 2. Overall, it is evident from Fig. 4 and Table 2

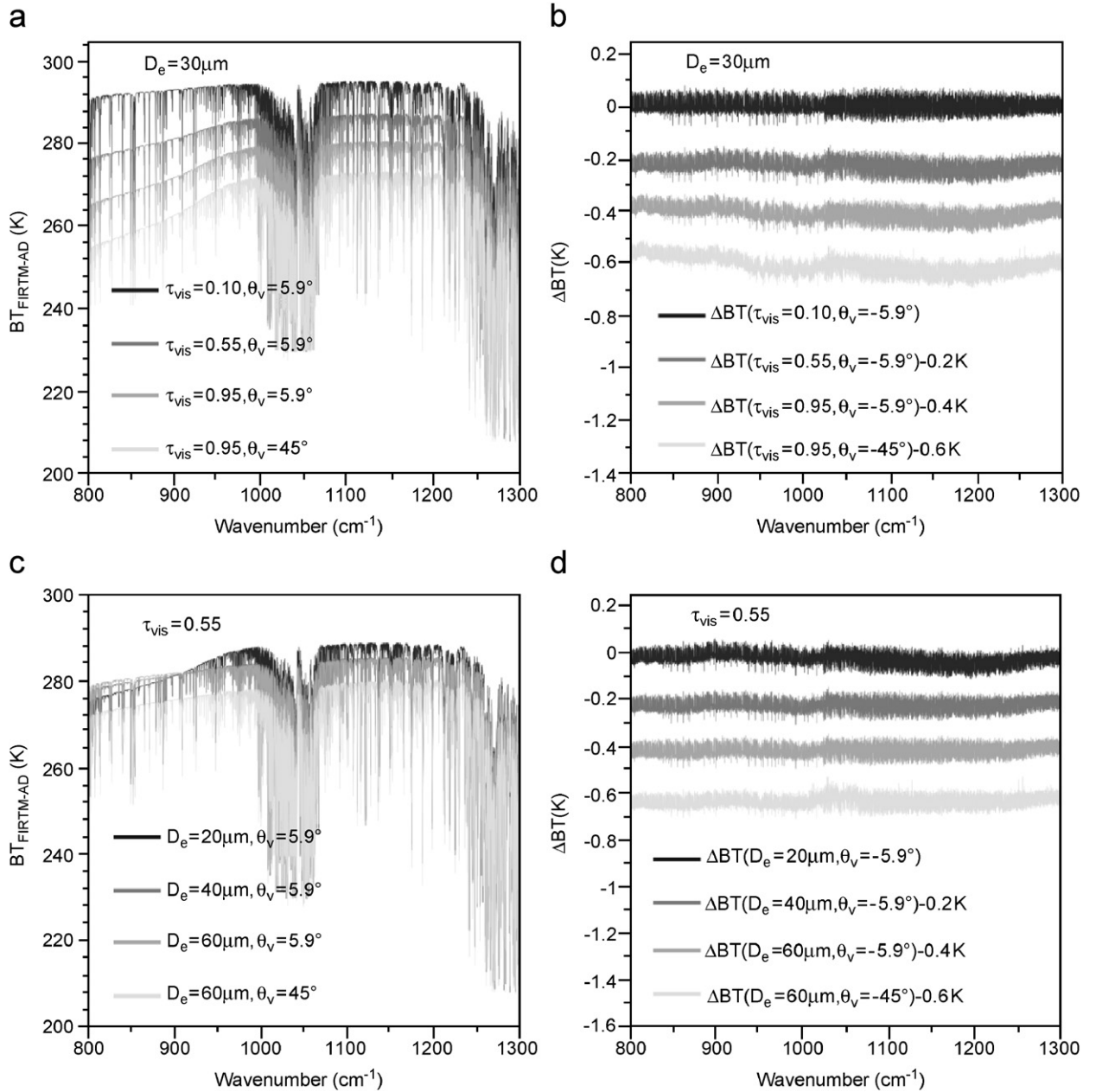


Fig. 4. Application of FIRTm-AD to hyperspectral BT computations at TOA for single-layered clouds. (a) BT spectra at TOA from FIRTm-AD for various combinations of cloud-visible optical thicknesses, τ_{vis} , and viewing angles, θ_v , while the cloud particle effective size, D_e , is $30 \mu\text{m}$ in all scenarios. (b) The differences in BT spectra between FIRTm-AD and DISORT ($\Delta\text{BT} = \text{BT}_{\text{FIRTm-AD}} - \text{BT}_{\text{DISORT}}$) in the scenarios shown in (a). (c) BT spectra at TOA from FIRTm-AD for various combinations of D_e and θ_v , while $\tau_{\text{vis}} = 0.55$ in all scenarios. (d) ΔBT spectra corresponding to the scenarios shown in (c). The RMS values of the ΔBT spectra in (b) and (d) are listed in Table 2.

that the accuracy of FIRTm-AD in the computations of BT spectra for optically thin single-layered cirrus cloud is very good. The error of FIRTm-AD in this type of application is an order of magnitude smaller than that of FIRTm1 and FIRTm2, and also well below the NEdT of the current advanced hyperspectral sensors.

In addition to the satellite-based hyperspectral sensors, the ground-based hyperspectral sensors, such as the AERI, are also important application areas for FIRTm-AD. Fig. 5 shows the application of FIRTm-AD to

Table 2

RMS BT errors of FIRTM-AD with respect to DISORT under the single-layered cloud conditions in the scenarios shown in Fig. 4 and the major error sources present in each scenario

Scenario #	τ_{vis}	D_e (μm)	θ_v (deg)	Error sources ^a	RMS of ΔBT (K)
1	0.10	30	5.9	(1), (2)	0.0306
2	0.55	30	5.9	(1), (2), (3)	0.0426
3	0.95	30	5.9	(1), (2), (3)	0.0334
4	0.95	30	45.0	(1), (2), (3), (4)	0.0365
5	0.55	20	5.9	(1), (2), (3)	0.0448
6	0.55	40	5.9	(1), (2), (3)	0.0422
7	0.55	60	5.9	(1), (2), (3)	0.0372
8	0.55	60	45.0	(1), (2), (3), (4)	0.0498

^a(1) Cloud realization error; (2) v -interpolation error; (3) τ -interpolation error; (4) μ -interpolation error.

the computations of BT spectra corresponding to the downwelling radiances at the surface. The cloud configurations for the results shown in Fig. 5 are the same as those in Fig. 4. Fig. 5a shows the BT spectra computed from FIRTM-AD for various combinations of τ_{vis} and θ_v . The corresponding ΔBT spectra are shown in Fig. 5b. The BT spectra for various combinations of D_e and θ_v are shown in Fig. 5c with corresponding ΔBT spectra shown in Fig. 5d. Note that a negative viewing angle indicates the viewing direction is upward at the surface; the absolute value of the angle corresponds to the angle between the nadir and viewing direction. The RMS BT errors of FIRTM-AD in all scenarios, as shown in Fig. 5b and d, are quite featureless. The RMS values of ΔBT in all scenarios are smaller than 0.03 K.

Fig. 6 shows the errors of FIRTM-AD for a two-layered cirrus cloud case. The upper layer is located in a layer from 11.5 to 12 km above the surface with a cloud top and base temperature of 225.5 and 228.5 K, respectively. The τ_{vis} and D_e of the upper layer are assumed as 1.25 and 30 μm , respectively. The lower cirrus layer is located at 11–11.5 km with a top and base temperature of 228.5 and 231.75 K, respectively. Because Figs. 4 and 5 reveal that the accuracy of FIRTM-AD has little dependence on D_e , only a single effective particle size, $D_e = 100 \mu\text{m}$, is assumed for the lower layer. Fig. 6a shows the differences between FIRTM-AD and DISORT in simulating the BT spectra at TOA, i.e., the ΔBT spectra at TOA, under various combinations of lower layer τ_{vis} (1.75, 2.75, 3.75) and downward viewing angles, θ_v (5.9° and 45°). The ΔBT spectra at the surface under various combinations of lower layer τ_{vis} and upward viewing angles (−5.9° and −45°) are shown in Fig. 6b. The RMS values of each ΔBT spectrum in Fig. 6 and the major error sources in each scenario are listed in Table 3. In comparison with the single-layered cloud case, the errors of FIRTM-AD applied to two-layered cloud are slightly larger (the largest error is about 0.06 K in the scenario #1 in Table 3). A small warm bias, which is caused by the use of the approximate cloud realization scheme described in Section 3 to treat the non-isothermal clouds, is observed in Fig. 6b indicating that FIRTM-AD tends to slightly overestimate the downwelling radiances at the surface. However, despite the bias, the largest error of FIRTM-AD in Fig. 6b (scenario #8 in Table 3) is still substantially smaller than 0.2 K.

Fig. 7 shows the errors of FIRTM-AD in the computation of nadir-viewing BT spectra for a case where there is a multilayered (three-layered) cirrus cloud in a tropical atmosphere. The uppermost cirrus layer is located between 13.5 and 14.0 km with τ_{vis} and D_e of 0.25 and 30 μm , respectively. The middle and lower layers are located, respectively, at 11.5–12 and 11.0–11.5 km. The τ_{vis} and D_e of the middle layer are 1.25 and 60 μm , respectively. The corresponding values for the lower layer are 1.75 and 100 μm , respectively. The RMS values of ΔBT spectra at TOA and surface are 0.0439 and 0.072 K, respectively.

6. Discussions and summary

The computational efficiency of FIRTM-AD depends on the optical thickness and extent of inhomogeneity of cloud layers. As mentioned in Section 3, the efficiency of FIRTM-AD is also affected by the value of τ^* . Based on the timing of the computations in the above error analyses, the computational efficiency of FIRTM-AD when τ^* is set to 20 under the single, double and multilayered cloud conditions is listed in Table 4 along

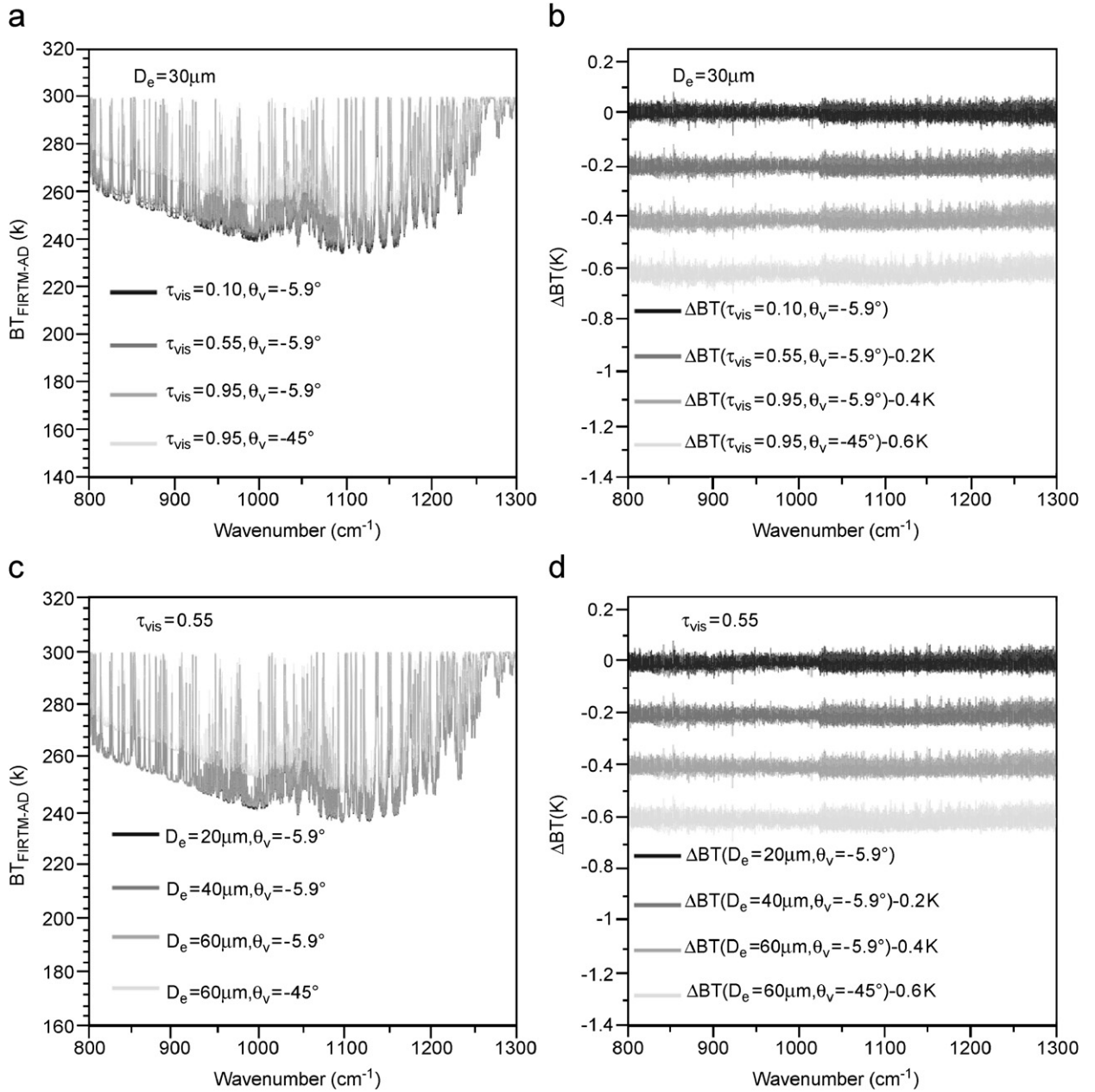


Fig. 5. Application of FIRTm-AD to hyperspectral BT computations at the surface for single-layered cloud conditions. (a) BT spectra at the surface from FIRTm-AD for various combinations of τ_{vis} and θ_v , while $D_e = 30 \mu\text{m}$. (b) ΔBT spectra corresponding to the scenarios shown in (a). (c) BT spectra at the surface from FIRTm-AD for various combinations of D_e and θ_v , while $\tau_{\text{vis}} = 0.55$ in all scenarios. (d) ΔBT spectra corresponding to the scenarios shown in (c).

with that of DISORT under the same conditions. For the type of computations in Figs. 4 and 5, the FIRTm-AD is approximately 250 times faster than DISORT. Under three-layered cloud conditions as in Fig. 6, FIRTm-AD is still more than two orders of magnitude faster than DISORT. Given that the instrument noise level of current hyperspectral sensors, such as AIRS and IASI, is about 0.2 K, the RMS errors of FIRTm-AD for the cases shown in the previous section are quite acceptable. However, there are endless combinations of potential cloud and viewing conditions and therefore it is almost certain that the errors of FIRTm-AD will

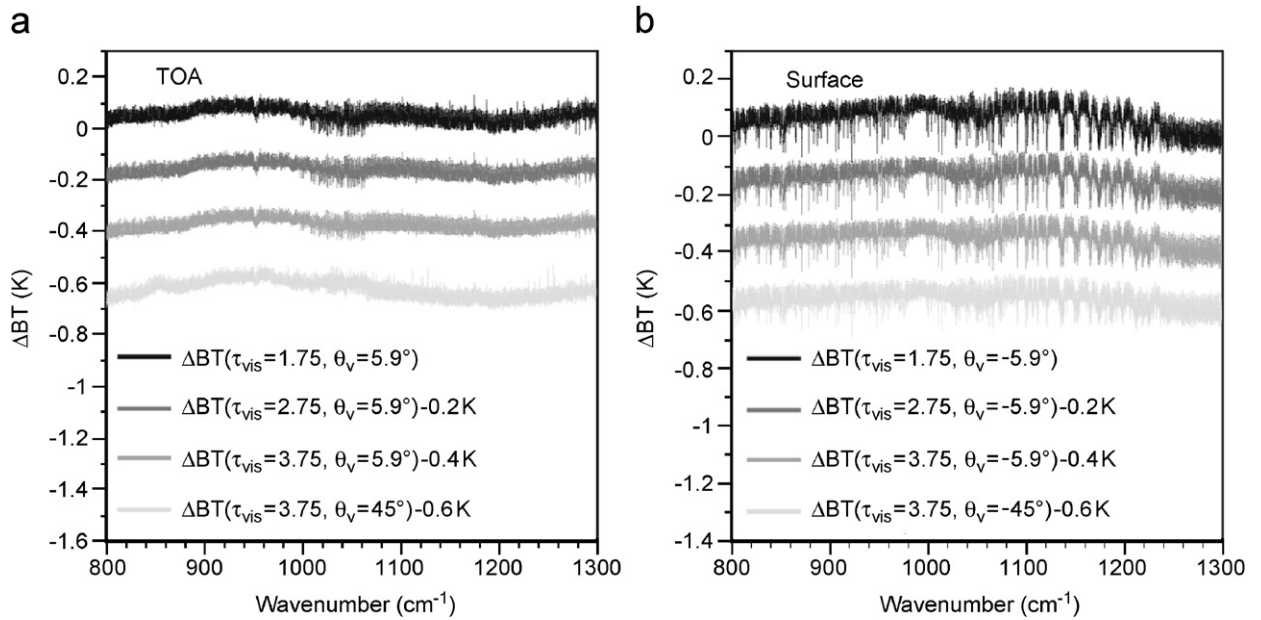


Fig. 6. The errors of FIRTM-AD in hyperspectral BT computations for a two-layered cirrus cloud. The τ_{vis} and D_e of the upper cirrus layer are, respectively, 1.25 and 30 μm . The D_e of the lower cirrus layer is 100 μm . (a) ΔBT spectra at TOA for various combinations of lower cirrus layer τ_{vis} and θ_v values. (b) ΔBT spectra for various combinations of lower cirrus layer τ_{vis} and θ_v . The RMS values of ΔBT are listed in Table 3.

Table 3

RMS BT errors of FIRTM-AD with respect to DISORT under the two-layered cloud condition in the scenarios shown in Fig. 6 and the corresponding major error sources

Scenario #	τ_{vis}	D_e (μm)	θ_v (deg)	Error sources ^a	RMS of ΔBT (K)
1	1.75	100	5.9	(1), (2), (3)	0.0583
2	2.75	100	5.9	(1), (2), (3)	0.0490
3	3.75	100	5.9	(1), (2), (3)	0.0379
4	3.75	100	45.0	(1), (2), (3), (4)	0.0419
5	1.75	100	-5.9	(1), (2), (3)	0.0530
6	2.75	100	-5.9	(1), (2), (3)	0.0627
7	3.75	100	-5.9	(1), (2), (3)	0.0716
8	3.75	100	-45.0	(1), (2), (3), (4)	0.0812

^a(1) Cloud realization error; (2) v -interpolation error; (3) τ -interpolation error; (4) μ -interpolation error.

exceed 0.1 K in some extreme cases. Given the algorithms used in the formulation of FIRTM-AD, it is unlikely that the accuracy of FIRTM-AD will substantially degrade in those cases. We believe that the errors of the FIRTM-AD in those cases are unlikely to exceed those of FIRTM1 and FIRTM2. Also, it is necessary to point out that in the above simulations the solar contribution has been ignored in both FIRTM-AD and DISORT. Future work is planned to investigate the impact of this omission under different cloud conditions and sun-satellite angles.

It is worth noting that FIRTM-AD is applicable not only to the hyperspectral sensors, but also to the narrowband sensors in the thermal IR spectral region. For the remote sensing of cloud properties using bispectral narrowband satellite measurements in the thermal IR region (e.g., 8–12 μm), which is independent of solar illumination, the cloud signatures in the atmospheric window region are often used to derive their properties. Fig. 8 shows an example of the LUT generated using one channel at 11 μm (a bandwidth, 10.78–11.28 μm , corresponding to MODIS channel #31 is assumed) and the other channel at 12 μm

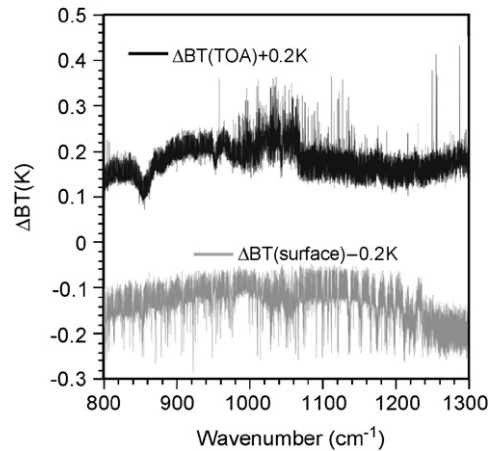


Fig. 7. The errors of FIRTm-AD for a case where there are three layers of cirrus cloud in the atmosphere shown in Fig. 3. The black line corresponds to the ΔBT spectrum at TOA (downward nadir viewing) with the values shifted upward by 0.2 K. The gray line corresponds to the ΔBT spectrum at the surface (upward nadir-viewing) with the values shifted downward by 0.2 K.

Table 4

Computational efficiencies (in seconds per 100 wavenumbers) of FIRTm-AD and DISORT under the same conditions on an Apple 1.8 GHz G5 computer^a

Cloud conditions	DISORT (32-stream)	FIRTm-AD (32-stream)
Single-layered (Figs. 4 and 5)	53.775	0.231
Two-layered ^b (Fig. 6)	56.342	0.434
Three-layered (Fig. 7)	57.012	0.526

^aIn FIRTm-AD, τ^* is set to 20 in all simulations.

^b τ_{vis} of the lower layer is 3.75.

(a bandwidth, 11.77–12.27 μm , corresponding to MODIS channel #32 is assumed). This kind of LUT has been used to retrieve the cloud thermodynamic phase [58] and is also potentially useful for the inference of τ_{vis} and D_e of ice clouds at night. As shown in Fig. 8, one dimension of the table is the BT at 11 μm and the other is the difference in BT between 11 and 12 μm . Each point in the table corresponds to an ice cloud with a unique combination of τ_{vis} and D_e . Along each solid line, from right to left, the D_e of the cloud remains constant while τ_{vis} increases. Along each dashed line, from top to bottom, the τ_{vis} remains constant while the D_e increases. This feature of the table has made it possible to infer τ_{vis} and D_e by projecting the instrument measurements onto the table. An important point to note is that this kind of LUT depends on the atmospheric profile and therefore must be renewed often because the temperature and water vapor profiles can change from one footprint to another. Moreover, for each footprint the RT model has to be run dozens of times to generate a LUT as shown in Fig. 8. Consequently, a practical implementation of this approach requires computationally efficient RT models, which makes the generation of these LUTs a useful application for FIRTm-AD. The asterisk points in Fig. 8 are obtained with DISORT and the points marked as circles are results from FIRTm-AD. In the simulations, the tropical atmosphere shown in Fig. 3 is used. The optical thickness profile of the background atmosphere is obtained from the correlated k -distribution model developed by Kratz [59]. It is seen from the figure that the two groups of points completely overlap, indicating the equivalence of the two models in terms of the accuracy for this retrieval algorithm. However, the CPU requirements with FIRTm-AD are much less than with DISORT.

In summary, based on the advantages of CHARTS, FIRTm1 and FIRTm2, we have developed a fast IR RT model based on the well-known adding–doubling principle for applications to the forward RT simulations involved in the hyperspectral remote-sensing applications under cloudy-sky conditions. Because of the use of the pre-computed LUT, the computational burden associated with the doubling process is substantially

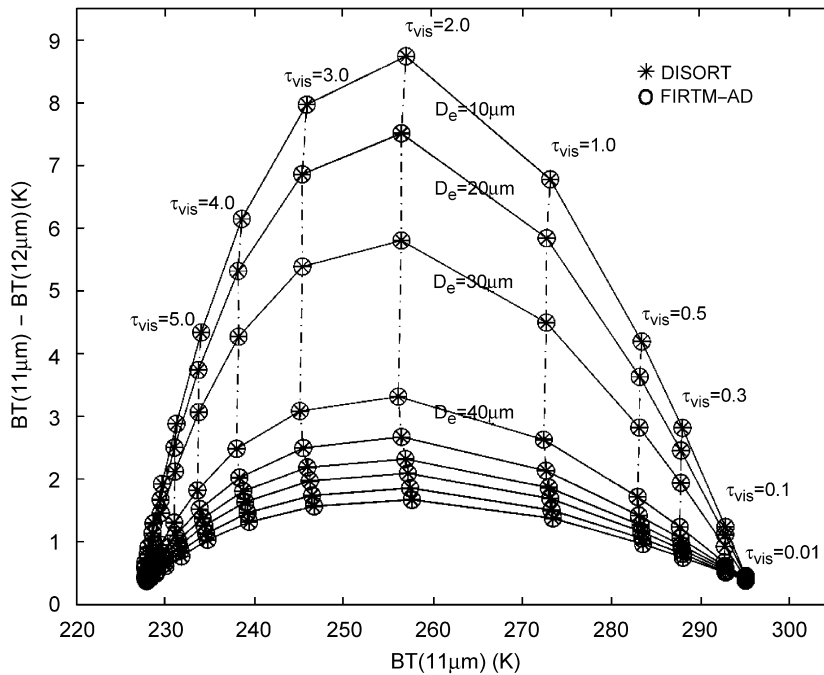


Fig. 8. A look-up table for the cloud property retrieval using 11- and 12 μm channels. Along each solid line, from right to left, the optical thickness of the cloud increases while the effective size remains constant. Along each dashed line, from top to bottom, the effective size of the cloud increases while the optical thickness remains constant. The asterisks are results from DISORT and the circles are from FIRTM-AD.

alleviated in FIRTM-AD. In comparison with FIRTM1 and FIRTM2, FIRTM-AD is much more flexible and accurate. FIRTM-AD is applicable to multilayered, inhomogeneous and non-isothermal clouds. In addition, FIRTM-AD can be applied to computations at both TOA and the surface, and therefore applicable to both satellite and ground-based hyperspectral sensors. The comparisons have shown that FIRTM-AD is about 250 times faster than DISORT in the computations of BT spectra at TOA and the surface for a single-layered thin ($\tau_{\text{vis}} < 1$) cirrus cloud. The RMS BT errors of FIRTM-AD in this type of application are generally smaller than 0.05 K. For two- or three-layered thick ($\tau_{\text{vis}} > 1$) cloud conditions, FIRTM-AD is still about two orders of magnitude more efficient than DISORT and the error is on the order of 0.1 K.

Acknowledgments

We appreciate the anonymous reviewers for their valuable comments and constructive critics. This research is supported by the National Science Foundation (NSF) CAREER Award research grant (ATM-0239605) from the NSF Physical Meteorology Program (ATM-0239605) managed by Dr. Andrew Detwiler, and partially by a research grant from NASA (NNG04GL24G), and a subcontract issued by the University of Wisconsin-Madison to Texas A&M University. Prof. George Kattawar's efforts are supported by the Office of Naval Research under contracts N00014-02-1-0478 and N00014-06-1-0069. Regarding his efforts on the study of the optical and radiative properties of ice clouds, Ping Yang specifically acknowledges the support and encouragement of Drs. Donald Anderson and Hal Maring who manage the NASA Modeling, Analysis and Prediction (MAP) Program and Radiation Sciences Program at NASA Headquarters, respectively.

Appendix A. Application of the adding–doubling method to thermal IR RT

The adding–doubling method is a rigorous method that has been extensively used to deal with the RT problems in the plane-parallel atmospheres [32–40]. The basic concepts and derivations of the

adding–doubling method can be found in some classic books [39,60–62]. In this Appendix, we show the application of the adding–doubling method to the thermal IR RTs.

In the adding–doubling method, the bidirectional reflection (R) and transmission (T) function are two fundamental and important quantities. Consider a cloud with an optical thickness of τ and an effective size of D_e illuminated from above. The layer is homogenous in terms of scattering albedo ($\langle\varpi\rangle$) and phase function ($\langle P \rangle$). The intensity of incident radiation is $I_{\text{top}}^\downarrow(\mu', \phi')$, where μ' is the cosine of zenith angle and ϕ' is the azimuthal angle. According to the definitions of R and T , the reflected and transmitted intensity may be expressed as in terms of incident intensity as follows [60]:

$$I_{\text{top}}^\uparrow(\mu, \phi) = \frac{1}{\pi} \int_0^{2\pi} \int_0^1 R(\mu, \phi, \mu', \phi - \phi') I_{\text{top}}^\downarrow(\mu', \phi') \mu' d\mu' d\phi', \quad (\text{A.1a})$$

$$I_{\text{bottom}}^\downarrow(\mu, \phi) = \frac{1}{\pi} \int_0^{2\pi} \int_0^1 T(\mu, \phi, \mu', \phi - \phi') I_{\text{top}}^\downarrow(\mu', \phi') \mu' d\mu' d\phi', \quad (\text{A.1b})$$

where $I_{\text{top}}^\uparrow(\mu, \phi)$ and $I_{\text{bottom}}^\downarrow(\mu, \phi)$ are reflected and transmitted intensity at cloud top and bottom, respectively. In general cases, R and T are usually decomposed into Fourier series in terms of the relative azimuthal angle $\phi - \phi'$ [62] for the sake of numerical implementation, and each term in the series is treated independently in the adding–doubling process. However, because the thermal emission under plane-parallel conditions are azimuthally independent, and the azimuthally dependent solar contribution is usually neglected [14,16,26] in the spectral region considered in this work, i.e., 800–1300 cm^{-1} , only the zero-order moment of the Fourier expansion is needed in the present study. In other words, we can use the azimuthally averaged reflection and transmission functions defined as follows:

$$\bar{R}(\mu, \mu') = \frac{1}{2\pi} \int_0^{2\pi} R(\mu, \phi, \mu', \phi - \phi') d(\phi - \phi'), \quad (\text{A.2a})$$

$$\bar{T}(\mu, \mu') = \frac{1}{2\pi} \int_0^{2\pi} T(\mu, \phi, \mu', \phi - \phi') d(\phi - \phi'). \quad (\text{A.2b})$$

Subsequently, Eq. (A.1) reduces to

$$I_{\text{top}}^\uparrow(\mu) = 2 \int_0^1 \bar{R}(\mu, \mu') I_{\text{top}}^\downarrow(\mu') \mu' d\mu', \quad (\text{A.3a})$$

$$I_{\text{bottom}}^\downarrow(\mu) = 2 \int_0^1 \bar{T}(\mu, \mu') I_{\text{top}}^\downarrow(\mu') \mu' d\mu'. \quad (\text{A.3b})$$

Note that \bar{T} consists of two parts, the direct (\bar{T}_{direct}) and diffuse (\bar{T}_{diffuse}) transmission. T_{direct} can be found in the form:

$$\bar{T}_{\text{direct}}(\mu, \mu') = \frac{1}{2\mu'} \exp(-\tau/\mu') \delta(\mu - \mu'), \quad (\text{A.4})$$

where δ is the Dirac delta function. Eqs. (A.1)–(A.4) are defined with respect to incidence from above. Likewise, the azimuthally averaged bidirectional reflection and transmission for incident radiation coming from below, $I_{\text{bottom}}^\uparrow(\mu')$, are given by

$$I_{\text{bottom}}^\downarrow(\mu) = 2 \int_0^1 \bar{R}^*(\mu, \mu') I_{\text{bottom}}^\uparrow(\mu') \mu' d\mu', \quad (\text{A.5a})$$

$$I_{\text{top}}^\uparrow(\mu) = 2 \int_0^1 \bar{T}^*(\mu, \mu') I_{\text{bottom}}^\uparrow(\mu') \mu' d\mu', \quad (\text{A.5b})$$

where the superscript * denotes that the incident radiation comes from below.

The adding principle states that the bidirectional functions of the combined layer of two adjacent layers, one on top of the other, can be obtained through the following adding process [60]:

$$Q = \bar{R}_1^* \bar{R}_2, \quad (\text{A.6a})$$

$$S = \sum_{n=1}^{\infty} Q^n, \quad (\text{A.6b})$$

$$D = \bar{T}_1 + S \bar{T}_1, \quad (\text{A.6c})$$

$$U = \bar{R}_2 D, \quad (\text{A.6d})$$

$$\bar{R}_{12} = \bar{R}_1 + \bar{T}_1^* U, \quad (\text{A.6e})$$

$$\bar{T}_{12} = \bar{T}_2 D, \quad (\text{A.6f})$$

where the subscripts 1 and 2 refer to the upper and lower layer, respectively. Note that the product of two bidirectional functions in the above equations implies integration over the adjoining solid angle to account for the multiple-scattering effects. For example, an arbitrary $Z = XY$ in above equations is defined as [60]

$$Z(\mu, \mu') = 2 \int_0^1 X(\mu, \mu'') Y(\mu'', \mu') \mu'' d\mu''. \quad (\text{A.7})$$

Similar to Eq. (A.6), the solution for bidirectional functions of the combined layer for radiation from below may be written as follows [60]:

$$Q^* = \bar{R}_2 \bar{R}_1^*, \quad (\text{A.8a})$$

$$S^* = \sum_{n=1}^{\infty} (Q^*)^n, \quad (\text{A.8b})$$

$$U^* = \bar{T}_2^* + S^* \bar{T}_2^*, \quad (\text{A.8c})$$

$$D^* = \bar{R}_1^* U^*, \quad (\text{A.8d})$$

$$\bar{R}_{12}^* = \bar{R}_2^* + \bar{T}_2^* D^*, \quad (\text{A.8e})$$

$$\bar{T}_{12}^* = \bar{T}_1^* U^*. \quad (\text{A.8f})$$

The adding method may also be applied to account for the thermal emission. The thermal emission of the combined layer contributed by the upper layer can be obtained using the adding equations as follows [61]:

$$D_{E1} = E_1^* + S E_1^*, \quad (\text{A.9a})$$

$$U_{E1} = \bar{R}_2 D_{E1}, \quad (\text{A.9b})$$

$$E_{12} = E_1 + \bar{T}_1^* U_{E1}, \quad (\text{A.9c})$$

$$E_{12}^* = \bar{T}_2 D_{E1}, \quad (\text{A.9d})$$

where E_1 and E_1^* are, respectively, the upward and downward thermal emission from the upper layer, S is defined in Eq. (A.6b). Similarly, the contributions of the bottom layer to the thermal emission of the combined layer are in the forms [61]:

$$U_{E2} = E_2 + S^* E_2, \quad (\text{A.10a})$$

$$D_{E2} = \bar{R}_1^* U_{E2}, \quad (\text{A.10b})$$

$$E_{12} = \bar{T}_1^* U_{E2}, \quad (\text{A.10c})$$

$$E_{12}^* = E_2^* + \bar{T}_2 D_{E2}, \quad (\text{A.10d})$$

where E_2 and E_2^* are, respectively, the upward and downward thermal emission from the bottom layer, S^* is defined in Eq. (A.8b). The thermal emission of combined layer in a matrix format can be obtained by mathematical manipulation of Eqs. (A.9) and (A.10):

$$\begin{bmatrix} E_{12} \\ E_{12}^* \end{bmatrix} = \mathbf{A} \begin{bmatrix} E_1 \\ E_2 \\ E_1^* \\ E_2^* \end{bmatrix}, \quad (\text{A.11a})$$

where

$$\mathbf{A} = \begin{bmatrix} 1 & \bar{T}_1^* + \bar{T}_1^* S^* & \bar{T}_1^* \bar{R}_2 + \bar{T}_1^* \bar{R}_2 S & 0 \\ 0 & \bar{T}_2 \bar{R}_1^* + \bar{T}_2 \bar{R}_1^* S^* & \bar{T}_2 + \bar{T}_2 S & 1 \end{bmatrix}. \quad (\text{A.11b})$$

Note that because \mathbf{A} is temperature independent, the thermal emission of a non-isothermal cloud can be obtained using the doubling method as long as it is homogenous in terms of bulk scattering properties.

For the sake of numerical implementation of integral in Eq. (A.7), the discrete-ordinate approximation is usually used in the adding–doubling method. Under the approximation, the integral in Eq. (A.7) becomes [25,60]:

$$Z(\mu_i, \mu_j) = 2 \sum_k^N X(\mu_i, \mu_k) Y(\mu_k, \mu_j) \mu_k w_k, \quad (\text{A.12})$$

where μ_k and w_k are quadrature points and corresponding weights determined by the discretization scheme. One of the most widely used quadratures for ordinate discretization is the so-called double Gaussian quadrature [25], in which the abscissas μ_k are distributed symmetrically around 0.5 and clustered toward 0 and 1. Under the discrete-ordinate approximation, \bar{R} and \bar{T} become matrices, whereas E becomes a vector as follows:

$$\bar{\mathbf{R}}_{ij} = \bar{R}(\mu_i, \mu_j), \quad (\text{A.13a})$$

$$\bar{\mathbf{T}}_{ij} = \bar{T}(\mu_i, \mu_j), \quad i, j = 1, 2, 3, \dots, N, \quad (\text{A.13b})$$

$$\mathbf{E}_i = E(\mu_i), \quad (\text{A.13c})$$

where μ_i is the cosine of the zenith angle of, respectively, reflected, transmitted and emitted radiation in the case for $\bar{\mathbf{R}}$, $\bar{\mathbf{T}}$ and \mathbf{E} . μ_j is the cosine of the zenith angle of incident radiation. N is the number of the points that the hemisphere $0 < \mu \leq 1$ is discretized into. Note that $2N$ is the so-called “number of streams”. Eq. (A.12) can be further simplified by defining a matrix operator as follows:

$$\mathbf{Z} = \mathbf{X} \otimes \mathbf{Y} = 2 \sum_{k=1}^N \mathbf{X}_{i,k} \mathbf{Y}_{k,j} \mu_k w_k, \quad i, j = 1, 2, 3, \dots, N. \quad (\text{A.14})$$

The last obstacle in the way of numerical implementation of the adding method is the infinite series in Eqs. (A.6b) and (A.8b). It has been shown that the infinite series can be efficiently treated as follows [61]:

$$\mathbf{S} = \mathbf{Q} \otimes (\mathbf{I} - \mathbf{Q})^{-1}, \quad (\text{A.15})$$

where \mathbf{I} is the identity matrix in the sense that $\mathbf{I} \otimes \mathbf{I} = \mathbf{I}$, and $(\cdot)^{-1}$ is the inverse operator such that $\mathbf{X} \otimes \mathbf{X}^{-1} = \mathbf{I}$. By substituting Eqs. (A.14) and (A.15) into the adding equations in Eqs. (A.6), (A.8) and (A.11), the adding process becomes a series of matrix operations and therefore can be easily implemented with the matrix manipulation subroutines from numerical linear algebra packages like LAPACK [63].

The adding method described above requires that the $\bar{\mathbf{R}}$, $\bar{\mathbf{T}}$ and \mathbf{E} be known for the layers to be added. To obtain the $\bar{\mathbf{R}}$, $\bar{\mathbf{T}}$ and \mathbf{E} of a cloud, homogenous in terms of bulk scattering properties, the doubling method can be used. In the method, the cloud is divided into a large amount of identical sub-layers. The sub-layers are optically thin ($\tau \sim 2^{-10}$) [45–47] so that their $\bar{\mathbf{R}}$, $\bar{\mathbf{T}}$ and \mathbf{E} can be obtained analytically. The properties of the whole cloud are obtained through a process in which two identical sub-layers are added at each step, i.e., the doubling process.

Appendix B. Interpolation scheme for FIRTM-AD to obtain radiances at the user-specified angles from model outputs

To obtain the radiances at the user-specified viewing angles from the model outputs at the quadrature points, an angular interpolation scheme is needed. There are numerous other schemes for the angular interpolation [38,39,64]. In the current FIRTM-AD, the following scheme is used. The radiances at model angles are first expanded as a series of the “shifted” Legendre polynomial [65]:

$$I(\tau; \mu) = \sum_{l=1}^M (2l+1) \chi_l(\tau) \bar{P}_l(\mu) \quad (\text{B.1a})$$

and

$$\chi_l(\tau) = \int_0^1 I(\tau; \mu) \bar{P}_l(\mu) d\mu, \quad (\text{B.1b})$$

where χ_l is the expansion coefficient of the l th moment and \bar{P}_l is the “shifted” Legendre polynomial analogous to the Legendre polynomials, but defined on the interval $[0,1]$ and obeying the orthogonality relationship:

$$\int_0^1 \bar{P}_m(\mu) \bar{P}_n(\mu) d\mu = \frac{1}{2n+1} \delta_{mn}, \quad (\text{B.2})$$

where δ_{mn} is the Kronecker delta. The expansion coefficient χ_l can be found by substituting the radiances at the quadrature points into Eq. (B.1b). And then the radiances at the user-specified angles are estimated using Eq. (B.1a).

References

- [1] Aumann HH, Chahine MT, Gautier C, Goldberg MD, Kalnay E, McMillin LM, et al. AIRS/AMSU/HSB on the Aqua mission: design, science objectives, data products, and processing systems. *IEEE Trans Geosci Remote Sensing* 2003;41:253–64.
- [2] Bloom HJ. The Cross-Track Infrared Sounder (CrIS): a sensor for operational meteorological remote sensing. *Int Geosci Remote Sensing Symp* 2001;3:1341–3.
- [3] Siméoni D, Singer C, Chalon G. Infrared atmospheric sounding interferometer. *Acta Astronaut* 1997;40:113–8.
- [4] Blumstein D, Chalon G, Carlier T, Buil C, Hébert P, Maciaszek T, et al. IASI instrument: technical overview and measured performances. *SPIE* 2004;5543:22, 2004.
- [5] Knuteson RO, et al. Atmospheric emitted radiance interferometer. Part I: instrument design. *J Atmos Oceanic Technol* 2004;21:1763–76.
- [6] Knuteson RO, et al. Atmospheric emitted radiance interferometer. Part II: instrument performance. *J Atmos Oceanic Technol* 2004;21:1777–89.
- [7] McMillin LM, Kleespies TJ, Crone LJ. Atmospheric transmittance of an absorbing gas. 5. Improvements to the OPTRAN approach. *Appl Opt* 1995;34:8396–9.
- [8] Strow LL, Hannon SE, De Souza-Machado S, Motteler HE, Tobin D. An overview of the AIRS radiative transfer model. *IEEE Trans Geosci Remote Sensing* 2003;41:303–13.
- [9] Moncet JL, Uymin G, Snell HE. Atmospheric radiance modeling using the optimal spectral sampling (OSS) method. *Proc SPIE* 2004;5425:368–74.
- [10] Liu X, Smith WL, Zhou DK, Larar A. Principal component-based radiative transfer model for hyperspectral sensors: theoretical concept. *Appl Opt* 2006;45:201–9.
- [11] Saunders R. A global comparison of HIRS and AVHRR radiances. In: 11th International ATOVS Study Conference, vol. 1, 2000. p. 345.
- [12] Goldberg MD, Qu Y, McMillin LM, Wolf W, Zhou L, Divakarla M. AIRS near-real-time products and algorithms in support of operational numerical weather prediction. *IEEE Trans Geosci Remote Sensing* 2003;41:379–89.

- [13] Li J, Liu CY, Huang HL, Schmit TJ, Wu X, Menzel WP, et al. Optimal cloud-clearing for AIRS radiances using MODIS. *IEEE Trans Geosci Remote Sensing* 2005;43:1266–78.
- [14] Li J, Huang HL, Liu CY, Yang P, Schmit TJ, Wei H, et al. Retrieval of cloud microphysical properties from MODIS and AIRS. *J Appl Meteorol* 2005;44:1526–43.
- [15] Wei H, Yang P, Li J, Baum BA, Huang H-L, Platnick S, et al. Retrieval of semitransparent ice cloud optical thickness from Atmospheric Infrared Sounder (AIRS) measurements. *IEEE Trans Geosci Remote Sensing* 2004;42:2254–67.
- [16] Saunders RW, Matricardi M, Brunel P. An improved fast radiative transfer model for assimilation of satellite radiance observations. *QJRM* 1999;125:1407–25.
- [17] Zhou DK, Smith WL, Liu X, Larar AM, Mango SA, Huang HL. Physically retrieving cloud and thermodynamic parameters from ultraspectral ir measurements. *J Atmos Sci* 2006 (accepted for publication).
- [18] Inoue T. On the temperature and effective emissivity determination of semi-transparent cirrus clouds by bi-spectral measurements in the 10- μ m window region. *J Meteor Soc Japan* 1985;63:88–99.
- [19] Inoue T. A cloud type classification with NOAA-7 split-window measurements. *J Geophys Res* 1987;92:3991–4000.
- [20] Wu MLC. A method for remote sensing the emissivity, fractional cloud cover and cloud top temperature of high-level, thin clouds. *J Appl Meteorol* 1987;26:225–33.
- [21] Parol F, Buriez JC, Brogniez G, Fouquart Y. Information content of AVHRR channels 4 and 5 with respect to the effective radius of cirrus cloud particles. *J Appl Meteorol* 1991;30:973–84.
- [22] Ou SC, Liou KN, Gooch WM, Takano Y. Remote sensing of cirrus cloud properties using AVHRR 3.7 and 10.9 μ m channels. *Appl Opt* 1993;32:2171–80.
- [23] Minnis P, Liou KN, Takano Y. Inference of cirrus cloud properties using satellite-observed visible and infrared radiances. Part I: parameterization of radiance fields. *J Atmos Sci* 1993;50:1279–304.
- [24] Minnis P, Garber DP, Young DF, Arduini RF, Takano Y. Parameterizations of reflectance and effective emittance for satellite remote sensing of cloud properties. *J Atmos Sci* 1998;55:3313–39.
- [25] Stamnes K, Tsay SC, Wiscombe WJ, Jayaweera K. Numerically stable algorithm for discrete-ordinate-method radiative transfer in multiple scattering and emitting layered media. *Appl Opt* 1988;27:2502–9.
- [26] Niu J, Yang P, Huang H-L, Davies JE, Li J, Baum BA, et al. A fast infrared radiative transfer model for overlapping clouds. *JSRT* 2007;103:447–59.
- [27] Chandrasekhar S. *Radiative transfer*. Oxford: Oxford University Press; 1950.
- [28] Liou KN. A numerical experiment on Chandrasekhar's discrete-ordinate method for radiative transfer: application to cloudy and hazy atmospheres. *J Atmos Sci* 1973;30:1303–26.
- [29] Evans KF. The spherical harmonic discrete ordinate method for three-dimensional atmospheric radiative transfer. *J Atmos Sci* 1998;55:429–46.
- [30] Collins DG, Blattner WG, Wells MB, Horak HG. Backward Monte Carlo calculations of the polarization characteristics of the radiation emerging from spherical shell atmospheres. *Appl Opt* 1972;11:2684–96.
- [31] Plass GN, Kattawar GW. Monte-Carlo calculation of light scattering from clouds. *Appl Opt* 1968;7:669–704.
- [32] Twomey S, Jacobowitz H, Howell HB. Matrix methods for multiple-scattering problems. *J Atmos Sci* 1966;23:289–98.
- [33] Hansen JE, Hovenier JW. The doubling method applied to multiple scattering of polarized light. *JSRT* 1971;11:809–12.
- [34] Lacis AA, Hansen JE. A parameterization for the absorption of solar radiation in the earth's atmosphere. *J Atmos Sci* 1974;31:118–33.
- [35] Irvine WM. Diffuse reflection and transmission by cloud and dust layers. *JSRT* 1974;8:471–85.
- [36] van de Hulst HC. *Multiple light scattering. Tables, formulas and applications*. New York: Academic Press; 1980.
- [37] Hansen JE. Multiple scattering of polarized light in planetary atmospheres. Part II sunlight reflected by terrestrial water clouds. *J Atmos Sci* 1971;28:1400–26.
- [38] de Haan JF, Bosma PB, Hovenier JW. The adding method for multiple scattering calculations of polarized light. *Astron Astrophys* 1987;183:371–91.
- [39] Hovenier JW, Van der Mee C, Domke H. *Transfer of polarized light in planetary atmospheres—basic concepts and practical methods*. Dordrecht, The Netherlands: Kluwer; 2004.
- [40] Moncet JL, Clough SA. Accelerated monochromatic radiative transfer for scattering atmospheres: Application of a new model to spectral radiance observations. *J Geophys Res* 1997;102:21853–66.
- [41] Wylie DP, Menzel WP. Eight year of high cloud statics using HIRS. *J Climate* 1999;12:170–84.
- [42] Wylie DP, Menzel WP, Wolf HM, Strabala KI. Four years of global cirrus cloud statistics using HIRS. *J Climate* 1994;7:1972–86.
- [43] Liou KN. Influence of cirrus clouds on weather and climate processes: a global perspective. *Mon Weather Rev* 1986;114:1167–99.
- [44] Lynch DK, Sassen K, Starr DO, Stephens D, editors. *Cirrus*. New York: Oxford University Press; 2002.
- [45] Wiscombe WJ. Extension of the doubling method to inhomogeneous sources. *JSRT* 1976;16:477–89.
- [46] Wiscombe WJ. On initialization, error and flux conservation in the doubling method. *JSRT* 1976;16:637–58.
- [47] Wiscombe WJ. Doubling initialization revised. *JSRT* 1977;18:245–8.
- [48] Slingo A. A GCM parameterization for the shortwave radiative properties of water clouds. *J Atmos Sci* 1989;46:1419–27.
- [49] Ebert EE, Curry JA. A parameterization of ice cloud optical properties for climate models. *J Geophys Res* 1992;97:3831–6.
- [50] Sassen K, Campbell JR. A midlatitude cirrus cloud climatology from the facility for atmospheric remote sensing. Part I: macrophysical and synoptic properties. *J Atmos Sci* 2001;58:481–96.
- [51] Huang HL, Yang P, Wei H, Baum BA, Hu Y, Atonelli P, et al. Inference of ice cloud properties from high-spectral resolution infrared observations. *IEEE Trans Geosci Remote Sensing* 2004;42:842–52.

- [52] Luo Z, Rossow WB. Characterizing tropical cirrus life cycle, evolution, and interaction with upper-tropospheric water vapor using Lagrangian trajectory analysis of satellite observations. *J Atmos Sci* 2004;17:4541–63.
- [53] Baum BA, Heymsfield AJ, Yang P, Bedka ST. Bulk scattering models for the remote sensing of ice clouds. Part 1: microphysical data and models. *J Appl Meteor* 2005;44:1885–95.
- [54] Baum BA. Personal communication <http://modis-atmos.gsfc.nasa.gov/products_C005update.html>.
- [55] Wiscombe WJ. The delta-M method: rapid yet accurate radiative flux calculations for strongly asymmetric phase functions. *J Atmos Sci* 1977;34:1408–22.
- [56] Gaiser SL, Aumann HH, Strow LL, Hannon SE, Weiler M. In-flight spectral calibration of the Atmospheric Infrared Sounder. *IEEE Trans Geosci Remote Sensing* 2003;41:287–97.
- [57] Clough SA, Iacono MJ, Moncet JL. Line-by-line calculations of atmospheric fluxes and cooling rates: application to water vapor. *J Geophys Res* 1992;97:15761–85.
- [58] Baum BA, Soulen PF, Strabala KI, King MD, Ackerman SA, Menzel WP, et al. Remote sensing of cloud properties using MODIS Airborne Simulator imagery during SUCCESS. II. Cloud thermodynamic phase. *J Geophys Res* 2000;105:11781–92.
- [59] Kratz DP. The correlated k-distribution technique as applied to the AVHRR channels. *JQSRT* 1995;53:501–17.
- [60] Liou KN. An introduction to atmospheric radiation. New York: Academic Press; 2002.
- [61] Goody RM, Young YL. Atmospheric radiation. New York: Oxford University Press; 1989.
- [62] Lenoble J. Radiative transfer in scattering and absorbing atmospheres: standard computational procedures. Hampton: A. Deepak; 1985.
- [63] Anderson E, et al. LAPACK Users' Guide. Philadelphia: Society for Industrial and Applied Mathematics; 1995.
- [64] Mishchenko MI, Dlugach JM, Yanovitskij EG, Zakharova NT. Bidirectional reflectance of flat, optically thick particulate layers: an efficient radiative transfer solution and applications to snow and soil surfaces. *JQSRT* 1999;63:409–32.
- [65] Abramowitz M, Stegun IA, editors. Handbook of mathematical functions with formulas, graphs, and mathematical tables, 9th printing. New York: Dover; 1972.